Analysis and Experimental Research on a Novel Multi-Contact MVDC Natural Current Commutation Breaking Topology

BOWEN JIA [1], **JIANWEN WU** [1], **(Senior Member, IEEE), SHANGWEN XIA**[1], **XIAOWU LUO**[1], **SULIANG MA** [1], **(Graduate Student Member, IEEE), AND YUAN JIANG** [2], **(Member, IEEE)**
[1]School of Automation Science and Electrical Engineering, Beihang University, Beijing 100083, China
[2]School of Automation and Electrical Engineering, University of Science and Technology Beijing, Beijing 100083, China

Corresponding author: Jianwen Wu (wujianwen@buaa.edu.cn)

ABSTRACT The high performance of medium-voltage direct current (MVDC) power supply system is a pre-requisite for several industrial applications. To meet the higher voltage direct current (DC) breaking requirements in the fields of aviation, aerospace, and new energy, this article proposes a novel MVDC commutation breaking topology that combines a load-carrying branch and an arcing branch in parallel. In contrast to the conventional structure based on semiconductor devices, each branch in the proposed topology contains a mechanical contact, which provides a lower on-state loss and higher voltage-breaking capacity. Moreover, the theoretical analysis and experimental results verified the asynchronous operation of the current-loading and confirmed that the arcing branch can realize the natural commutation of the current for the breaking of overload current or short-circuit current. A detailed equivalent model that combines the micro-electrical contact theory and phase-change characteristics of the electrode material was then established to investigate the molten metal bridge and pseudo arc phenomenon of the contact area during the commutation process. The results indicated that although the presence of a molten metal bridge and pseudo arc increase the current commutation time and erosion of the electrode material, the commutation process can be conducted. Finally, based on the softening voltage of the electrode material under the rated conditions, in addition to the phase change during dynamic commutation, the roughness σ and elastic modulus E can be adjusted appropriately to achieve arc-less current commutation.

INDEX TERMS Contact resistance, current commutation, dc circuit breaker, molten bridge.

I. INTRODUCTION

The medium-voltage direct current (MVDC) power supply system has received significant research attention in the aerospace, urban rail transit, new energy vehicles, and maritime transport fields. Such systems are characterized by low losses, simple control, accurate adjustments, and large power density. As critical devices, high-power DC contactors are essential for the induction, sustenance, and breaking of electrical circuits, with the exception of short circuit currents. Hence, their breaking characteristics have a significant influence on the system performance [1]–[4]. Several professional electrical manufacturing companies recently developed high-power DC contactor products, which operate at voltages of up to 1800 V and are therefore suitable for

aerospace and military applications. As there is no current zero-crossing point during DC breaking, specialized methods are required to extinguish the arc, such as the superimposition of the metal grid voltage drop, increase in the electric field strength of the arc column, lengthening of the arc, and generation of an artificial current zero-crossing [5]–[7]. Current commutation from the load current path to the commutation path is a pre-condition for the successful interruption of current in hybrid circuit breakers (HCBs). The resonance circuit in a conventional HCB is composed of a mechanical switch (MS) and an LC resonance circuit connected in parallel, which can redirect the switch current. Then the MS can then operate under zero current within several tens of microseconds [8]–[10]. An alternative solution is based on the cascading of semiconductor devices to achieve high-voltage and large-current circuit breaking. Although this type of circuit breaker can rapidly

The associate editor coordinating the review of this manuscript and approving it for publication was Bernardo Tellini [.]

achieve circuit breaking, the switching on-state loss, which is dependent on the semiconductor devices' characteristics, is generally large. Besides, the manufacture and maintenance costs are relatively high [11]. The HCB that combines the respective advantages of the mentioned methods is generally composed of three branches, namely, the load-carrying branch, commutation branch, and energy absorption branch. The load-carrying branch is typically composed of a MS with a small conduction loss. In particular, the current commutates from the MS to the commutation branch due to a different DC breaking topology [12]. With the omission of the snubber circuit, decrease in the current change rate, and increase in transient recovery voltage rate before zero-current, a cascaded commutation circuit and a parallel LC branch series with a thyristor were used to improve the fault current interruption capacity in [13] and [14]. Moreover, the circuit breaker (CB) characterized by the commutation of a short-circuit current from the load-carrying branch to the auxiliary branch based on rapid and precise current control by the multilevel pulse-width modulation (PWM) converter allows for the elimination of active semiconductor devices from the load current branch [15]. Similarly, a novel hybrid DC circuit breaker (DCCB) can achieve automatic current commutation from the mechanical switch to the semiconductor switch, using a series-coupled inductor during the breaking process [16]. After the replacement of the LC component of the self-oscillation auxiliary branch with an insulated-gate bipolar transistor (IGBT), thyristor, two inductors, and a grounding resistor, the proposed DCCB in [17] exhibited rapid responses and low power losses. Similarly, the current commutation drive circuit (CCDC) in [18] and [19], wherein the capacitor in the commutation path was not pre-charged and the reactor was removed, allowed for a simpler and more reliable charging system and current commutation method for the novel mechanical DCCB. The experimental results verified that a current of 3.4 kA can be commutated within 100 μs and be interrupted within 2 ms [20]. The commutation branch in the HCB topology includes a semiconductor device and its control circuit. In the commutation process, the control circuit drives the semiconductor device to conduct at a sustained voltage that generates an arc discharge between metal contacts, which results in the ablation of the electrode material. An arc-less commutation process uses the molten metal bridge voltage at the opening stage of the contacts, as demonstrated in [21]. The results revealed that a larger contact diameter, slow separation speed, and small commutation cable inductance are suitable for the improvement of the threshold current in arc-less commutation.

The investigation of the erosion is essential, considering the dynamic changes of the surface micro-topography of the electrode material during the breaking process. The general assumption is that the effective area of contact between two nominally flat metal surfaces is determined by the plastic deformation of their highest asperities, especially, when the height of the asperity is subject to a specific distribution law [22]. Moreover, the number of contact spots, total conductance, contact area, and load can be calculated using a set of formulae. This provides a simple multi-scale framework that can magnify the mechanism of tip contact to a rough macro surface. A rough surface was modeled as an ensemble of asperities with identical curvature radii and height distributions in [23] based on the double-Hertz and multiple asperity contact theories. An alternative method involves the use of the finite element method for the investigation of asperity interaction effects [24]. A numerical simulation was established in [25], with the determination of the structural deformations, voltage, and temperature distributions during contact separation. The erosion of the arc on the electrode material has a direct influence on the contact effect of the circuit breaker after re-closing. The eroded pit decreases the dielectric strength between the electrodes. Moreover, it increases the contact resistance and contact voltage drop. This leads to the formation of a molten metal bridge, which causes the contact to melt [26]. In [27], a mathematical model was presented for the calculation of the welding dynamics during contact closure and breaking, which describes the dynamics of the contact temperature at the pre-melting stage and the evolution of the welding zones.

In summary, the direct cascading of the switchgear to increase the voltage level will limits the current level due to the rated temperature. At the same time, the single-break structure is limited by the breaking voltage. In addition, the HCB is constrained by the complex structure and large size, which does not meet the breaking requirements of medium voltage and large current in compact applications. At present, the DC switchgear produced by mainstream electrical appliance manufacturers, such as GIGAVAC/HX460, TE Connectivity/K1K06X, and TDK/HVC500 adopt a sealed contact structure without a transfer branch. Each switching process results in the ablation of the metal material on the contact surface, thus minimizing the service life. This article therefore proposes a novel multi-contact MVDC natural current commutation breaking topology. Compared with conventional hybrid topology and existing switchgear, the proposed topology is advantageous in that the commutation branch does not contain semiconductor devices and transistors. In addition, it exhibits the following characteristics:

1) The load-carrying branch conducts a large proportion of the rated current, due to the design of the contact overtravel between different branch contacts.

2) Due to the asynchronous disconnection between different branch contacts, the current is naturally commutated and rapidly interrupted during the breaking process.

3) Since the circuit breaking process will not cause ablation to the contacts of the load-carrying branch, the number of breaking actions will hardly effect the rated current. The bidirectional circuit breaking function of the same capacity can be realized through the design of the arc blowing magnetic field.

The structure of the paper is organized as follows. Section II introduces the proposed topology structure and
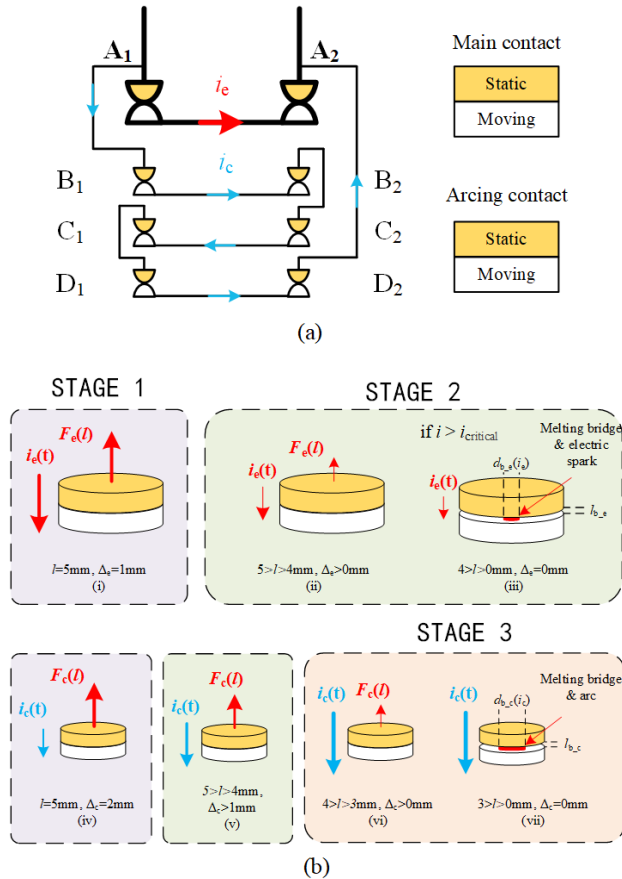
FIGURE 1. Schematic diagram of each stage of the commutation process: (a) connection structure between different branches, and (b) changes in contact state with respect to armature displacement *l*.

an analysis of the natural current commutation process. In section III, the proposed topology is verified with respect to the realization of current commutation based on the experimental results of the principle prototype. Section IV establishes and verifies a model for the investigation of the dynamic characteristics of the commutation process. In section V, the relationship between the generation and rupture of molten bridges in the contact area and the contact material parameters is detailed, which serves as a basis for the minimization of material erosion. Section VI summarizes the conclusions of the study.

II. TOPOLOGY STRUCTURE DESIGN OF CONTACT STRUCTURE

The circuit-breaking process of the multi-contact MVDC natural current commutation consists of three stages; namely the load-carrying stage, the natural commutating stage, and the arcing stage.

Fig. 1(a) presents the state of each branch of the prototype and the internal current distribution at the load-carrying stage. The contact structure comprises a load-carrying branch (A1-A2) and an arcing branch (B1-B2-C2-C1-D1-D2) connected in parallel. Moreover, i_e and i_c represent the current that flows through the load-carrying branch and arcing branch, respectively. Considering that the contact material

TABLE 1. Assembly parameters of each branch of contacts.

Symbol	Description	Value
d_e	Diameter of the load-carrying branch contact	18 mm
h_e	Opening distance of the load-carrying branch	4 mm
Δ_e	Overtravel of the load-carrying branch	1±0.2 mm
F_e	Final force of the load-carrying contact	60 N
d_c	Diameter of the arcing branch contact	10 mm
h_c	Opening distance of the arcing branch	3 mm
Δ_c	Overtravel of the arcing branch	2±0.2 mm
F_c	Final force of the arcing contact	36 N
v	Average opening speed	0.7 m/s

does not soften when carrying a current of 2000 A (for copper, $U_j < 0.12$ V) within a specified margin, the contact voltage drop was determined to be 33–50% of the softening voltage. The contact resistance $R_j < 0.03$ mΩ was obtained. According to the empirical formula $R_j = K_j/(0.102F)^m$, when m $= 1$ and $K_j = 0.14$, the contact force F_e of the load-carrying branch was approximately 60 N. For the arcing branch, given that it is in parallel with the load-carrying branch, a certain proportion of the rated current is conducted when it is switched on. The ratio of the arcing branch current can be reduced by decreasing the contact force, which can help reduce the on-state loss. Therefore, the contact force F_c of the arcing branch was set as approximately 30 N. The diameter of the contact was determined according to the standard of the current carrying density of the conductor (5–8 A/mm²), the experimental test results of assembly parameters were obtained. The assembly parameters of each branch-contacts are presented in Table 1. At present, the parameters in Table 1 are the initial reference values. If there is ablation of the load-carrying branch contacts during the commutation process (this is undesirable), further experiments are required to dynamically adjust the parameters in Table 1.The load-carrying branch contains a set of double-break contacts with large diameters and large spring stiffness values; Thus, the contact resistance of the load-carrying contact is low in the switching-on state. Similarly, the arcing branch is composed of three sets of double-break semicircular shaped contacts connected in series, with relatively small diameters and spring stiffness values, which significantly increases the contact resistance.

Due to the differences in the overtravel and the spring stiffness values between different branches of the contact, the current is distributed and inversely proportional to the resistance of each branch at the load-carrying stage. Fig. 1(b) details the specific detailed breaking process of each stage.

At the load-carrying stage (STAGE 1), Fig.1(b-i, iv) reveals that a large proportion of current flows through the load-carrying branch, which reduces the contact voltage drop when the contactor is switched on. This solves the problem related to the increase in the temperature rise. Upon the induction

of the breaking process, the armature displacement l and the overtravel of each branch contact (Δ_e, Δ_c) gradually decrease. In the natural commutating stage (STAGE 2), the insulated connecting rod, which is driven by the electromagnetic operating mechanism, achieves the simultaneous action of each branch contact. The difference in the contact overtravel induces changes in the contact resistances of different branches, which results in the natural commutation of the current in the load-carrying branch to the arcing branch, as shown in Fig.1 (b-ii, v). Moreover, as shown in Fig.1 (b-iii), when the current exceeds the critical current, the significant amount of Joule heat accumulated on the electrode material results in a phase transition of the surface material near the time when Δ_e becomes zero. Molten metal bridges or pseudo arc prolong the commutation time and ablate the material of the load-carrying contacts to an extent. In the early arcing stage (STAGE 3), as shown in Fig.1(b-vi), a specific overtravel of the arcing contacts maintain the circuit conduction state for a short period of time. Thereafter, as shown in Fig.1(b-vii), with the action of the operating mechanism, the overtravel of the arcing branch gradually decreases, and arcs are generated in sequence. Finally, since 4 atm of hydrogen is sealed in the arc extinguishing chamber as the arc extinguishing medium, arcs are rapidly extinguished under the action of the magnetic blowing system and the gas atmosphere in the interrupter, thus completing the breaking process.

III. EXPERIMENTAL VERIFICATION OF THE PRINCIPLE PROTOTYPE

To verify the feasibility of the proposed multi-contact MVDC natural commutation breaking topology, the assembled principle prototype and a circuit schematic shown in Fig. 2(a) were employed for experimental verification.

The experimental circuit consisted of a pre-charged capacitor C_1 (capacitance and withstand voltages are 1/4 F and 1200 V, respectively), a sampling resistor R_s, a prototype K, a resistive load R_L, a large current-conducting gate turn-off (GTO) thyristor, and a line equivalent inductance L_1. The circuit discharge time constant was 250 ms. Since experimental power supply was provided by the energy storage capacitor, the voltage of the capacitor decayed exponentially with respect to the time constant of the experimental loop during the discharge process. To verify the breaking characteristics of the topology at given current and voltage levels, the circuit discharge time maintained at less than 25 ms, i.e., the pre-charged capacitor voltage drops not exceed 10%. It was therefore necessary to add a sufficiently large current-conducting GTO thyristor to accurately control the current introduction time. By matching the opening time of the prototype, a short-time discharge of the circuit could be realized to satisfy the experimental conditions of the specific voltage and large current.
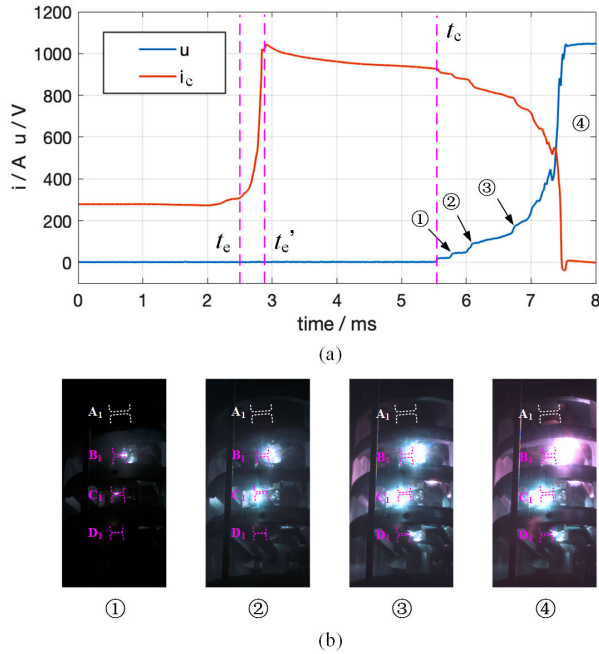
The experimental environment on site is shown as Fig.2(b), the GTO continuous current circuit was composed of C_2 and R_2. The current i_2 generated by the capacitor C_2 that
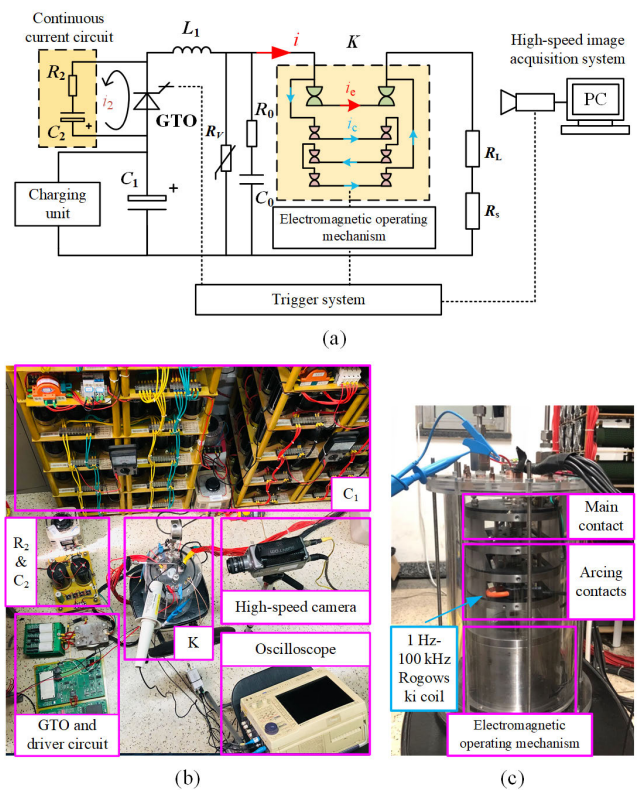
FIGURE 2. Schematic of the experimental circuit: (a) circuit topology, (b) the experimental environment on site, and (c) the assembled contactor prototype.

discharges the resistor R_2 can maintain the GTO conduction state when the current is small; Thus, the post-arc recovery voltage was applied across the contacts to ensure the equivalence of experimental results. At the same time, the switchable GTO thyristor was switched off after the circuit was connected for a specific amount of time. Moreover, when the contactor prototype did not complete the normal breaking, the GTO thyristor protected the device in the circuit. The absorption circuit composed of R_0, C_0, and R_V was used absorb the residual energy in the post-arc period and suppress the generation of overvoltage. A high-speed camera (Phantom v7.3) was used to capture arc appearance at a rate of 120,000 fps and exposure time of 1 μs. The total current i and the arcing branch current i_c were directly measured using a non-inductive sampling resistor R_s and miniature Rogowski coil with a bandwidth of 1Hz–100kHz, successively. A high voltage Tektronix P6015A probe was then used to measure the voltage across the contactor. Fig. 2(c) shows the appearance of the assembled contactor, the different branches of contacts are vertically distributed in space. The waveform and arc evolution pattern of the prototype breaking operation when connected to a resistive load at 1100 V and 1000 A is presented in Fig.3. Moreover, the arcing branch voltage and current waveforms were recorded in the commutating and arcing stage.

In the current commutation stage, the current in the arcing branch increased from 270 A to 1032 A, in accordance with
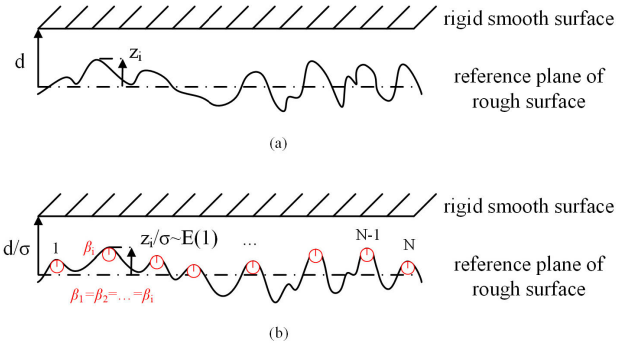
FIGURE 4. Contact between a rigid smooth surface and randomly rough surface: (a) A real case and (b) an equivalent model of the height of asperities that satisfying exponential distribution.

FIGURE 3. Experimental results of DC resistive load (1100 V, 1000 A) breaking: (a) voltage and current waveforms of arcing branch during breaking, and (b) arc appearance at each of the arcing contacts. ① The first arcing contacts open ② the second arcing contacts open ③ the third arcing contacts open and ④ maximum arc power moment.

the change in the armature displacement. When $t = t_e$, the insulated connecting rod collided with the moving contact, and the damping force generated by the material penetration partially counteracted the contact force. At the instant $t = t_e$', the contact of the load-carrying branch was separated. Since there were no significant changes in the contact voltage, the current commutation process was determined to be arc-less.

Subsequently, the contacts of the arcing branch were opened sequentially at times ①, ②, and ③ in Fig.3(a), and the arc appearance at the corresponding time is shown in Fig.3 (b). The electrode material of the contactor prototype was pure copper, with a minimum arc voltage U_{copper} of 13 V [28]. An assumption was made that electrons emitted from the cathode are accelerated by a voltage toward the anode, and that they possess sufficient energy upon reaching the anode to ionize the hydrogen in the anode area for the further generation of free electrons and resulting potential difference. This voltage is equal to the ionization potential (in Volts), thus the ionization potential of hydrogen in the interrupter U_{H2} was 13.54 V. The initial voltage between each contact is composed of the minimum arc voltage and gas arc voltage drop, and the metal phase arc voltage was approximately $6 \times (U_{copper} + U_{H2}) = 159.24$ V for the arcing branch with 6 contacts in series, which is consistent with the voltage value near point ③. At point ④, the arc was at maximum power; however, it was unevenly distributed among the contacts of the arcing branch. Hence, the breakdown phenomenon could occur.

The underlying principle of the multi-contact breaking circuit of the arcing branch is natural current commutation.

Therefore, it is necessary to investigate the change rate of the arcing branch current i_c during the commutation process t_e-t_e'.

IV. ESTABLISHMENT AND VERIFICATION OF THE COMMUTATION PROCESS MODEL

This section presents a discussion on the establishment of the equivalent model of the commutation process based on the application of the micro-electrical contact theory, considering the phase change characteristics of the electrode material.

A. MICROSCOPIC ELECTRICAL CONTACT MODEL

In particular, the surface of the electrode is composed of a large number of highly random asperities at the micro-scale, which is not a completely smooth plane. Thus, the actual conductive area is significantly smaller than the macro-scale of the electrode. An effective microscopic representation of the electrode material is shown in Fig. 4 (a).

The two rough contact surfaces are equivalent to a rigid-smooth surface and another rough surface. A reference surface can be used to represent the average value of the rough surface. Moreover, when the separation distance d between the reference surface and the smooth surface is less than the asperity height z, the asperities with the original height greater than d will form conductive spots. Therefore, for any given asperity, the probability of the formation of a conductive spot can calculated by (1), where $\phi(z)$ is the probability density function of the height distribution.

$$prob(z > d) = \int_d^\infty \phi(z)dz \tag{1}$$

As shown in Fig. 4 (b), in this study, the following assumptions were made about a micro-electrical contact, and an equivalent model was established as follows: (1) The heights of all asperities on the rough surface were in accordance with an exponential distribution. Then, separation distance d and the asperity height z_i can be normalized, the minimum separation distance between the two reference planes is $d_{min} = \sqrt{\pi}\sqrt{\sigma\beta}$, and σ is the surface roughness of the electrode material. (2) The geometry at the top of each asperity is a hemisphere with the same radius β. (3) Upon contact, different asperities are independent of each other.

(4) The deformation of the junction area between the liquid metal bridge and the electrode is not considered.

According to the theory proposed by Greenwood and Williamson, the number of contact spots (n), total contraction conductance (G), actual contact area (A_b), and contact force (F) between the two contact surfaces during the breaking process can be calculated [22]. After derivation, the relationship between the contact resistance, actual contact area, and contact force was determined, as shown in (2).

$$\begin{cases} R_{\text{contact}} = \dfrac{1}{G} = \dfrac{\rho E \sigma \cdot e^h}{\sqrt{\pi} \eta E \beta^{1/2} \sigma^{3/2} A_a} = \dfrac{\rho E \sigma}{F} \\ A_b = \dfrac{\sqrt{\pi} \eta E \beta^{1/2} \sigma^{3/2} A_a \cdot \sqrt{\pi} \beta^{1/2}}{e^h E \sigma^{1/2}} = \dfrac{\sqrt{\pi} \beta^{1/2} F}{E \sigma^{1/2}} \end{cases} \quad (2)$$

When the insulated connecting rod collides with the moving contact during the opening process, the damping force generated by the material deformation partially counteracts the contact force. The insulated connecting rod causes the contacts to collide until the combined force between the contacts is zero. The contact force is formed by the superposition of the spring force F_s and the damping force F_m generated by the deformation. This article presents an impact function to express the damping force during the collision process, which can be expressed as (3), (4).

$$\begin{cases} F = F_s - F_m \\ F_m = F_{e0} \cdot step \end{cases} \quad (3)$$

$$step = \begin{cases} 1, & l < 4 - \delta \\ 1 - \Delta^2(3 - 2\Delta) & 4 - \delta < l < 4 \\ 0 & l > 4 \end{cases} \quad (4)$$

where F_{e0} is the initial force of the load-carrying contact spring, and δ is the material deformation depth. The collision process of the insulated connecting rod and the moving contact occurs when the armature displacement is 4 mm, $\Delta = (l - 4 + \delta)/\delta$.

B. ELECTRODE MATERIAL PHASE-CHANGE MODEL

During the current commutation process, the actual contact area between the electrode materials decreases in accordance with a decrease in the contact force, and a significant amount of Joule heat accumulates in the contact area. Since the distance between the electrodes is not enough to make the gas sealed in the arc extinguishing chamber fully surround the conductive area, the degree of convection heat dissipation is not apparent. If the radiation heat dissipation is not considered at the same time, the accumulated heat can only be dissipated via the electrode surface. When the contacting area temperature is greater than the melting temperature T_m of the electrode material, a phase-change process from the solid phase to the liquid phase is induced. The macro phenomenon of this process is the generation of a molten metal bridge, and with the continual increase in temperature, it is accompanied by a pseudo arc. Based on the principle of energy conservation, the difference equations (5) and (6) can be used to describe the material phase state in the contact area before
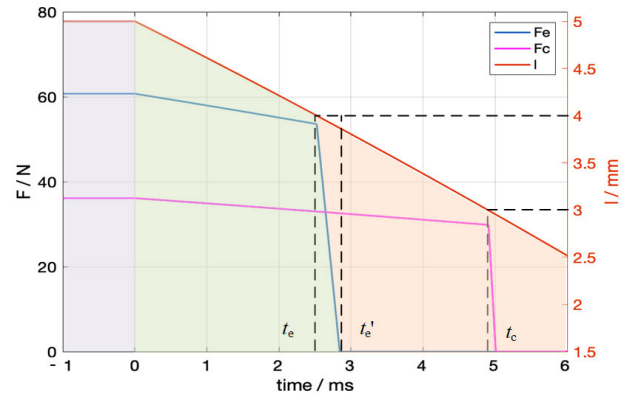

FIGURE 5. Relationship between contact force and armature displacement.

and after melting.

$$\begin{cases} c_P m_b (k) \, \Delta\tau (k) = \left(i_b^2 (k) R_b (k) - P_T (k) \right) \Delta t \\ m_b (k) = \gamma V_b (k) = \gamma A_b (k) \pi^{1/2} \sigma^{1/2} \beta^{1/2} \\ R_b (k) = \rho_0 (1 + \alpha \Delta T (k)) \dfrac{\pi^{1/2} \sigma^{1/2} \beta^{1/2}}{A_b (k)}, \\ \Delta T (k) < T_m \end{cases} \quad (5)$$

$$\begin{cases} c_P \, m_b|_{\Delta T = T_m} \Delta\tau (k) = \left(i_b^2 (k) R_b' (k) - P_T (k) \right) \Delta t \\ R_b' (k) = \dfrac{\rho_0 (1 + \alpha \Delta T (k)) \, m_b|_{\Delta T = T_m}}{\gamma A_b (k)^2}, \\ \Delta T (k) > T_m \end{cases} \quad (6)$$

where, c_p is the specific heat at the constant pressure of the metal material; Δt is the calculation step, which is equal to 1e-8 s; $\Delta\tau(k)$ is the increase in temperature of the metal material at each calculation step; ΔT, as obtained by the summation of $\Delta\tau(k)$, is the current temperature of the material, which is used to determine whether there is a phase-change of the electrode material during the commutation process. Moreover, γ is the material density, 8.9e3 kg/m³; ρ_0 is the resistivity at 273K, 1.75e-8 Ωm; α is the temperature coefficient of resistance, 4.1e-3 °C⁻¹.

The expression of the conducted dissipation power $P_T(k)$ is determined by (8), λ is the heat dissipation coefficient, 390 W/(m*K); and h is the material thickness, 20 mm.

$$\Delta T (k) = \sum_{k=1} \Delta\tau (k) \quad (7)$$

$$P_T (k) = \frac{2\lambda A_b (k) \Delta T (k)}{h} \quad (8)$$

C. COMPREHENSIVE MODEL ACCURACY VERIFICATION

The Simulink (MATLAB) toolbox was used to build the research model of the commutation process in accordance with the model established in the previous section. Fig. 5 indicates a piecewise linear relationship between the armature displacement and that the contact force of the load-carrying branch and the arcing branch. Moreover, R_e represents the contact resistance of the load-carrying branch, R_c is the contact resistance of the arcing branch, and formula (2) is used to establish the relationship with F_e and F_c.
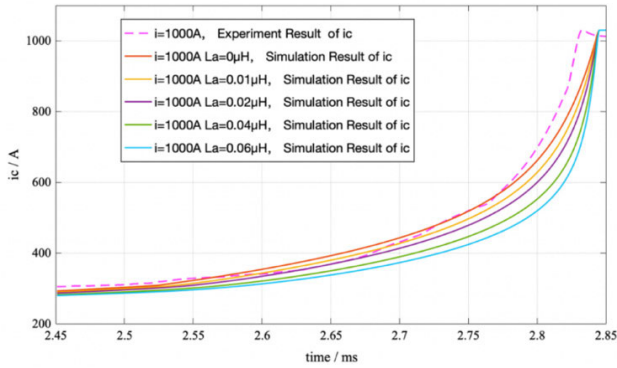
FIGURE 6. Experimental and simulation results of ic under different stray inductance La.
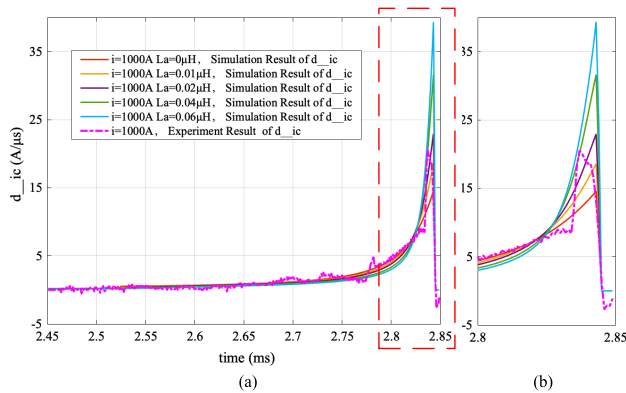

FIGURE 7. (a) Experimental and simulation results of the rate of increase in current during the commutation process, and (b) the partial magnification of the range from 2.8-2.85 ms.

The arcing branch is composed of three sets of double-break contacts connected in series using conductive elements. The conductive structure encloses a region in the space; thus, the stray inductance of the arcing branch has a significant influence on the commutation rate. The simulation model of the commutation process proposed in the previous section was used to simulate the results of the stray inductance La = 0 μH, 0.01 μH, 0.02 μH, 0.04 μH, and 0.06 μH at 1000 A. The simulation and experimental results of the arcing branch current i_c are shown in Fig 6.

Based on the simulation results, it was found that under the conditions of different branch stray inductances, the current commutation time is consistent. With an increase in the stray inductance L_a of the arcing branch, the rate of change in current at the later stage of the commutation stage increased significantly. Due to the deviation of the start time between the simulation model and the experimental results, the data required further processing.

Moreover, the derivative of the current waveform with respect to time was used to obtain the current growth rate during the commutation process. The delay time of the experimental and simulation results was determined as 14 μs using the correlation function. The current growth rate waveforms with the same start times are shown in the Fig. 7.

With an increase in L_a, the rate of increase in current significantly increased, and a relatively high over-voltage was generated before the end of the commutation process. The RMSE of the rate of increase in current of the experimental and simulated waveforms were calculated when the stray inductance L_a = 0 μH, 0.01 μH, 0.02 μH, 0.04 μH, 0.06 μH. The values were found to be 1.146 A/μs, 1.131 A/μs, 0.924 A/μs, 1.679 A/μs, and 2.354 A/μs, which verifies the accuracy of the simulation model, and the stray inductance parameter of the arcing branch is 0.02 μH.

V. ANALYSIS OF THE COMMUTATION PROCESS MODEL

According to the commutation process model and the branch distribution parameters established in the previous section, a series of commutation process simulations at different current levels were conducted. The simulation results of the contact district temperature, contact voltage drop, and current commutation process are shown in Fig. 8.

As can be seen from Fig. 8(a), with an increase in the commutation current, there was an increase in the temperature of the contact area. Because the heat between the contacts was dissipated by conduction via the electrodes, the Joule heat generated by the current increased the temperature of the electrode material continuously, which could result in a subsequent phase-change process. When the commutation current was 4000 A, the material in the contact area reached the melting temperature T_m at t_1 = 2.78 ms, and a metal liquid bridge was rapidly generated. Due to the negative resistance characteristic of the liquid metal bridge, there was a voltage drop, as shown in Fig. 8(b). The moving and static contacts of the load-carrying branch were then separated at t_3 = 2.84 ms for the formation of the contact gap distance. Since the temperature of the contact area was in excess of 4000 K at this instant, the high temperature resulted in the formation of a pseudo arc from the metal vapor. Thereafter, the metal vapor temperature reached a peak temperature of 9400K at time t_4, and the duration of the molten bridge and pseudo arc was Δt_1 = 0.97 ms. The same process occurred when the commutation current was 3000 A. At t_2 = 2.83 ms, the contact area reached the melting temperature T_m of the metal material, and a molten bridge was generated. The temperature of the metal vapor reached a peak value of 7800 K at time t_5, and the duration of the molten bridge and pseudo arc was Δt_2 = 0.73 ms.

Conversely, when the commutation current was less than 2000 A, the temperature of the contact area during the entire commutation process was less than the material melting temperature T_m. The energy stored in the stray inductance was rapidly absorbed at the instant of contact separation; thus, arc-less commutation was realized.

To prevent the erosion of the load-carrying branch contacts during the commutation process, the electrode material roughness σ (1.2 μm, 1.6 μm, 1.8 μm, 2 μm, and 2.4 μm) and the elastic modulus E (0.7 GPa, 0.9 GPa, 1.1 GPa, 1.3 GPa, and 1.5 GPa) were considered as the eigenvalues for the commutation simulation study. Fig. 9 presents the increase in temperature of the contact area.
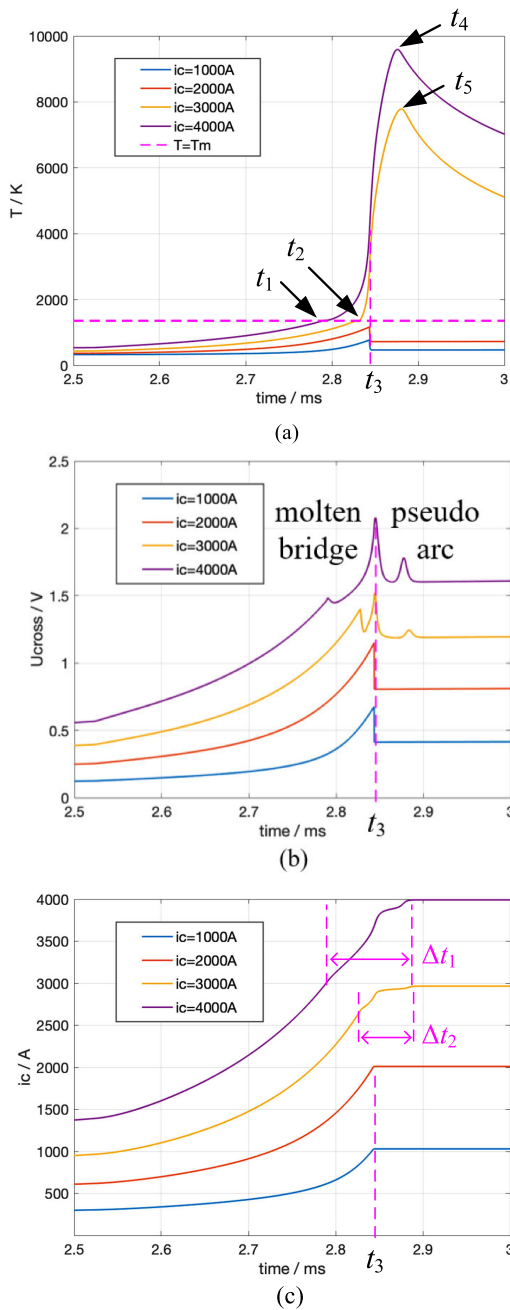
FIGURE 8. The temperature of the contact district at different current levels, (b) contact voltage drops at different current levels, and (c) current commutation process at different current levels.

Figs. 9 (a–d) present the temperature of the contact area when the contacts were separated (t_3 = 2.84 ms) at the current levels of 1000–4000 A, in increments of 1000 A, respectively. The projection of the surface with a temperature value lower than the material melting point T_m on the σ-E plane is represented by the gray area, thus indicating that the electrode material was not eroded during the commutation process. As can be seen from the figures, with an increase in the current level, the σ-E area where the electrode material parameters can be selected during arc-less commutation is significantly reduced. In particular, at 4000 A, there was none intersection between the temperature surface and the
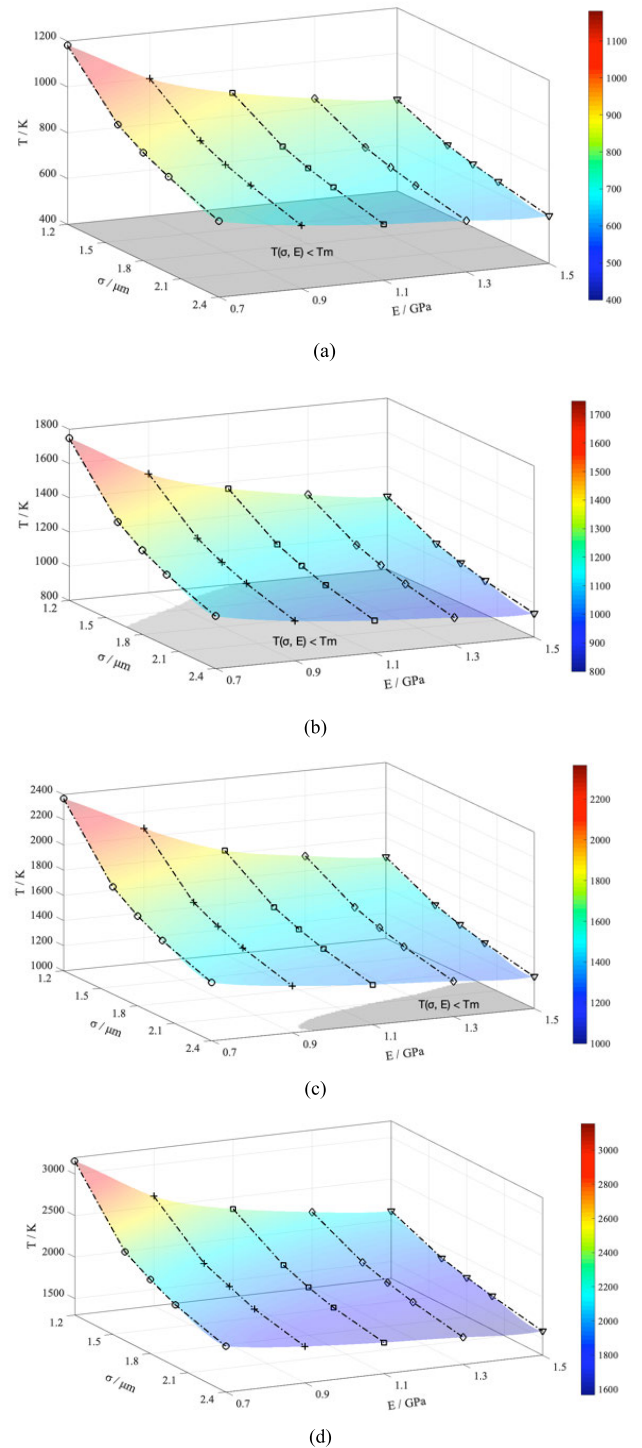
FIGURE 9. Temperature of the contact area upon the separation of the contacts at the current levels of (a) 1000 A, (b) 2000 A, (c) 3000 A, and (d) 4000 A.

critical surface. Although a rougher surface and a harder material can reduce the temperature of the contact area during commutation, the resulting rated heating of the contacts is excessive.

Moreover, under the rated condition of 1000 A, to ensure stable contact, the softening voltage U_m = 0.12 V of the copper material was set as the critical voltage. The simulation
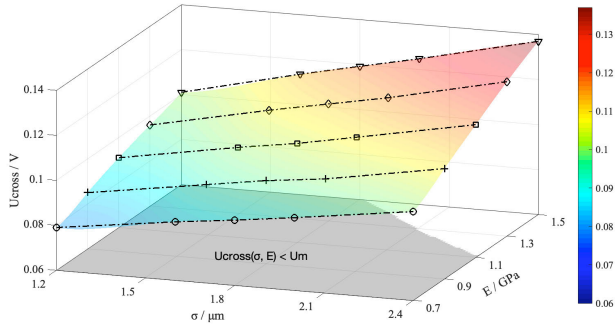
FIGURE 10. Relationship between contact voltage and the electrode material parameters at rated current of 1000 A.
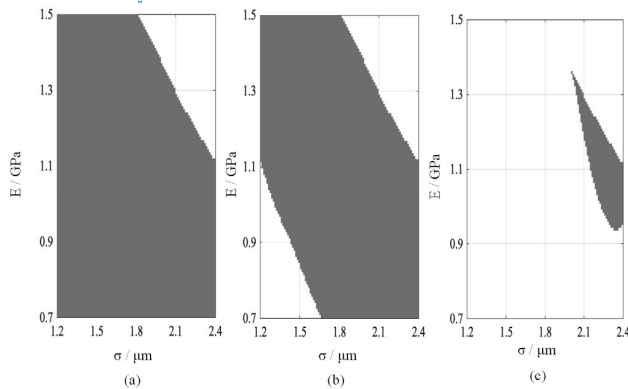

FIGURE 11. Electrode material parameter area for arc-less commutation at (a) 1000 A (b) 2000 A, and (c) 3000 A.

results of this reference voltage and the contact voltage were then analyzed with respect to different surface roughness σ and elastic modulus E values, as shown in Fig. 10. As can be seen from the figure, the projection of the surface where the contact voltage was lower than the softening voltage on the σ-E plane is represented by the gray area, thus indicating that the electrode material did not soften at a rated current of 1000A, and can conduct current stably.

Based on the combined ranges of the electrode material parameters shown in Figs. 9 and 10, an acceptable range for the surface roughness σ and elastic modulus E of the electrode material was determined, which can ensure contact reliability and prevent the electrode from softening during conduction at level the rated current. In addition, the temperature of the contact area was lower than the melting point, thus, an arc-less commutation process was realized.

For contactors, the breaking current is generally greater than the rated current by several factors. In the case of a resistive load with a rated current of 1000 A and breaking currents of 1000 A, 2000 A, and 3000 A, the parameter area of the electrode material for the realization of arc-less commutation is shown in Fig. 11. Besides, this area can be used to determine whether an arc is generated during commutation.

It should be noted that this criterion method is only applicable to the adjustment of a small current range. With an increase in the current level, i.e., to 4000A, arc-

TABLE 2. Parameter comparison between the proposed topology and the switchgear with similar breaking capacity.

	Band / Type	Max Voltage [V]	Max Current [A]	Switching life at max rating [Cycles]	Feature	Release time [ms]
1	GIGAVAC / HX460	1500	2700	2(1000V/2700A)	Bidirectional	<70
2	TDK / HVC500	1000	900	1(1000V/900A)	Bidirectional; Integrated sensors	<21.3
3	Littelfuse/ DCNEVT500	1800	500	1(1800V/500A)	Directional	--
4	TE / K1K06X	1000	1200	4(1000V/1200A)	Bidirectional	Typ.8
5	HF / HFE82V-600	800	2500	1(800V/2500A)	Bidirectional with different capacity	<30
6	Proposed topology	3000 expected	3000 expected	10(1000V/1000A)*	Bidirectional	<10

* Due to the limited capacity of energy storage capacitors in the laboratory, experiments with higher voltage levels will be carried out through subsequent synthetic experiments.

less commutation cannot be realized by the adjustment of the electrode material parameters. It is necessary to improve the contact system by an increase in the diameter of the contact, replacement of a spring with larger spring coefficient, and/or selection of a contact material with greater conductivity.

VI. CONCLUSION

This article proposes a multi-contact MVDC circuit breaking topological structure based on natural current commutation.

1) By the asynchronous operation of contacts in different branches, the natural current commutation from the load-carrying branch to the arcing branch can be realized. Thus, the forced current commutating branch of conventional hybrid topological structures can be removed. Moreover, the proposed topology can enhance the breaking capacity by increasing the contact number of the arcing branch. This provides alternative DC switching solutions for the aerospace, urban rail traction and new energy industries, which are sensitive to the volume and weight of the device.

2) An equivalent model combined with the microscopic electrical contact theory and impact collision process of the commutation stage is established and verified with the experimental data.

3) Under given conditions, a liquid metal bridge and spark discharge were formed during the natural commutation process. Although this prolonged the commutation time and increased the erosion of the contact material, current transfer between different branches was realized.

4) An acceptable range for the surface roughness σ and elastic modulus E of the electrode material was obtained based on the contact voltage drop at 1000 A and the phase-change law in the dynamic commutation process from 1000–4000 A. This serves as a theoretical basis for the optimization.

APPENDIX

Parameter comparison table of the proposed topology and the switchgear with similar breaking capacity is as Table 2.

REFERENCES

[1] Y. Shang, X. Li, H. Qian, S. Wu, Q. Pan, L. Huang, and Z. Jiao, "A novel electro hydrostatic actuator system with energy recovery module for more electric aircraft," *IEEE Trans. Ind. Electron.*, vol. 67, no. 4, pp. 2991–2999, Apr. 2020.

[2] C. Meyer, M. Kowal, and R. W. De Doncker, "Circuit breaker concepts for future high-power DC-applications," in *Proc. 14th IAS Annu. Meeting. Conf. Rec. Ind. Appl. Conf.*, 2005, pp. 860–866.

[3] X. Zhang, Z. Yu, Z. Chen, Y. Huang, B. Zhao, and R. Zeng, "Modular design methodology of DC breaker based on discrete metal oxide varistors with series power electronic devices for HVdc application," *IEEE Trans. Ind. Electron.*, vol. 66, no. 10, pp. 7653–7662, Oct. 2019.

[4] A. Mokhberdoran, D. Van Hertem, N. Silva, H. Leite, and A. Carvalho, "Multiport hybrid HVDC circuit breaker," *IEEE Trans. Ind. Electron.*, vol. 65, no. 1, pp. 309–320, Jan. 2018.

[5] X. Chao, W. Jianwen, L. Bin, and L. Peng, "Plasma characteristics of DC Hydrogen—Nitrogen mixed gas arc under high pressure," *IEEE Trans. Plasma Sci.*, vol. 42, no. 10, pp. 2722–2723, Oct. 2014.

[6] S. Teng, Z. Zhang, and L. Xiao, "Research on a novel DC circuit breaker based on artificial current zero-crossing," *IEEE Access*, vol. 8, pp. 36070–36079, 2020.

[7] L. Qu, Z. Yu, X. Xiao, W. Zhao, Y. Huang, and R. Zeng, "Development and application of a 10 kV mechanical DC circuit breaker," *Energies*, vol. 12, no. 19, p. 3615, Sep. 2019.

[8] L. Qu, Z. Yu, Y. Huang, and R. Zeng, "Research on effect of circuit parameters on breaking characteristics of mechanical DC circuit breaker," *Electr. Power Syst. Res.*, vol. 179, Feb. 2020, Art. no. 106075.

[9] S. Sen and S. Mehraeen, "Improving low-voltage DC circuit breaker performance through an alternate commutating circuit," *IEEE Trans. Ind. Appl.*, vol. 55, no. 6, pp. 6127–6136, Nov. 2019.

[10] K. Zhu, X. Li, S. Jia, W. Zhang, and W. Gao, "Study of the switching arc characteristics of a 500 kV HVDC self-excited oscillatory metallic return transfer breaker," *IEEE Trans. Dielectr. Electr. Insul.*, vol. 22, no. 1, pp. 128–134, Feb. 2015.

[11] Q. Song, R. Zeng, Z. Yu, W. Liu, Y. Huang, W. Yang, and X. Li, "A modular multilevel converter integrated with DC circuit breaker," *IEEE Trans. Power Del.*, vol. 33, no. 5, pp. 2502–2512, Oct. 2018.

[12] Y. Wu, Y. Wu, M. Rong, and F. Yang, "Development of a novel HVdc circuit breaker combining liquid metal load commutation switch and two-stage commutation circuit," *IEEE Trans. Ind. Electron.*, vol. 66, no. 8, pp. 6055–6064, Aug. 2019.

[13] Y. Shan, T. C. Lim, S. J. Finney, W. Guang, B. W. Williams, D. Holliday, and X. Ding, "Cascaded commutation circuit for a hybrid DC breaker with dynamic control on fault current and DC breaker voltage," *IET Power Electron.*, vol. 10, no. 6, pp. 676–686, May 2017.

[14] I. B. M. Taha, M. I. Mosaad, and M. G. Ashmawy, "Incorporating inductor-capacitor branch for thyristor-based DC fault current interruption," *Int. Trans. Electr. Energy Syst.*, vol. 30, no. 2, pp. 1–15, Feb. 2020.

[15] A. Suzuki and H. Akagi, "HVDC circuit breakers combining mechanical switches and a multilevel PWM converter: Verification by downscaled models," *IEEE Trans. Power Electron.*, vol. 34, no. 5, pp. 4259–4269, May 2019.

[16] X. Pei, A. C. Smith, O. Cwikowski, and M. Barnes, "Hybrid DC circuit breaker with coupled inductor for automatic current commutation," *Int. J. Electr. Power Energy Syst.*, vol. 120, Sep. 2020, Art. no. 106004.

[17] Q. Guo, M. Yoon, J. Park, and G. Jang, "Novel topology of DC circuit breaker and current interruption in HVDC networks," *IEEJ Trans. Electr. Electron. Eng.*, vol. 12, no. 4, pp. 465–473, Jul. 2017.

[18] W. Wen, Y. Wang, B. Li, Y. Huang, R. Li, and Q. Wang, "Transient current interruption characteristics of a novel mechanical DC circuit breaker," *IEEE Trans. Power Electron.*, vol. 33, no. 11, pp. 9424–9431, Nov. 2018.

[19] W. Wen, Y. Huang, B. Li, Y. Wang, and T. Cheng, "Technical assessment of hybrid DCCB with improved current commutation drive circuit," *IEEE Trans. Ind. Appl.*, vol. 54, no. 5, pp. 5456–5464, Sep. 2018.

[20] W. Wen, Y. Huang, Y. Sun, J. Wu, M. Al-Dweikat, and W. Liu, "Research on current commutation measures for hybrid DC circuit breakers," *IEEE Trans. Power Del.*, vol. 31, no. 4, pp. 1456–1463, Aug. 2016.

[21] K. Yasuoka, Y. Tsuboi, T. Hayakawa, and N. Takeuchi, "Arcless commutation of a hybrid DC breaker by contact voltage of molten metal bridge," *IEEE Trans. Compon., Package. Manuf. Technol.*, vol. 8, no. 3, pp. 350–355, Mar. 2018.

[22] J. A. Greenwood and J. B. P. Williamson, "Contact of nominally flat surfaces," *Proc. R. Soc. Lond. A, Math. Phys. Sci.*, vol. 295, no. 1442, pp. 300–319, 1966.

[23] W. Zhang, F. Jin, S. Zhang, and X. Guo, "Adhesive contact on randomly rough surfaces based on the double-hertz model," *J. Appl. Mech.*, vol. 81, no. 5, pp. 1–7, May 2014.

[24] S. Chandrasekar, M. Eriten, and A. A. Polycarpou, "An improved model of asperity interaction in normal contact of rough surfaces," *J. Appl. Mech.*, vol. 80, no. 1, pp. 1–8, Jan. 2013.

[25] Z. Tan, W. Guan, J. Guo, S. Chen, and C. Wang, "Mechanical, electrical, and thermal coupled-field simulation of a molten metal bridge during contact separation," *IEEE Trans. Compon., Package. Manuf. Technol.*, vol. 3, no. 6, pp. 960–966, Jun. 2013.

[26] C. Ou, R. Nakayama, S. Zen, and K. Yasuoka, "Influence of a short-duration arc on the erosion and dielectric strength of narrow air-gap contacts in a hybrid DC switch," *IEEE Trans. Compon., Package. Manuf. Technol.*, vol. 9, no. 6, pp. 1068–1074, Jun. 2019.

[27] S. N. Kharin, H. Nouri, and T. Davies, "The mathematical models of welding dynamics in closed and switching electrical contacts," in *Proc. 49th IEEE Holm Conf. Electr. Contacts*, 2003, pp. 107–123.

[28] P. G. Slade, *Electrical Contacts: Principles and Applications*, 2nd ed. New York, NY, USA: CRC Press, 2013, p. 586.

BOWEN JIA was born in Beijing, China, in 1992. He received the M.S. degree in electrical engineering from Beihang University, Beijing, in 2017, where he is currently pursuing the Ph.D. degree in electric machines and electric apparatus.

His research interests include arc fault diagnosis; plasma characteristics and the mechanism of dc arc interruption in hydrogen and mixed gases; the design of high-powered dc relays; and dc breaker technology.

JIANWEN WU (Senior Member, IEEE) received the B.S. and M.S. degrees in electrical engineering from the Shenyang University of Technology, Shenyang, China, in 1984 and 1987, respectively, and the Ph.D. degree in electrical engineering from Xi'an Jiaotong University, Xi'an, China, in 1995.

From 1995 to 1998, he was a Postdoctoral Fellow with the Huazhong University of Science and Technology, Wuhan, China. Since 2001, he has been a member of the faculty of the School of Automation Science and Electrical Engineering, Beijing, China, where he is currently a Professor. His research interests include vacuum arc theory, intelligent electrical apparatus, and power electronics technology. He is also a Senior Member of the China Electrotechnical Society (CES).

SHANGWEN XIA was born in Anhui, China, in 1992. He received the B.S. degree in electrical engineering from the Dalian University of Technology, in 2015, and the M.S. degree in electrical engineering from the Shenyang University of Technology, in 2019. He is currently pursuing the Ph.D. degree in electrical engineering with Beihang University. His current research interests include vacuum arc and electromagnetic operating mechanism.

XIAOWU LUO was born in Guangdong, China, in 1995. He received the B.S. degree in electrical engineering and its automation from Beihang University, Beijing, China, in 2018, where he is currently pursuing the M.S. degree in electrical engineering. His current research interests include intelligent electrical apparatuses and power electronics technology.

SULIANG MA (Graduate Student Member, IEEE) was born in Anshan, China, in 1988. He received the B.S. degree in electrical engineering and its automation and the M.S. degree in control engineering from the China University of Mining and Technology, Beijing, China, in 2011 and 2014, respectively. He is currently pursuing the Ph.D. degree in electric machines and electric apparatus with BUAA, Beijing.

From 2012 to 2013, he was a Graduate Student Researcher with the China Electric Power Research Institute (CEPRI), focusing on research, optimization, and design of the smart grid with wind, PV, and energy storage. His research interests include data-driven prognostics and health management for high-voltage switchgear, auto-measurement technology, control theory and application, and power electronics technology.

YUAN JIANG (Member, IEEE) was born in Dandong, China, in 1985. He received the B.S. and M.S. degrees in materials science and engineering and the Ph.D. degree in electrical engineering from Beihang University, Beijing, China, in 2008, 2011, and 2016, respectively.

From July 2016 to May 2017, he was with China North Industries Group Corporation. From May 2017 to June 2019, he was a Postdoctoral Fellow with Beihang University. He is currently a Lecturer with the University of Science and Technology Beijing. His research interests include the theory and application of avia-vacuum arcs, electrical appliances detection and fault diagnosis, intelligent micro-grid, and new energy technology.

. . .